Journal of
Materials Chemistry C

ROYAL SOCIETY
OF CHEMISTRY

PAPER

View Article Online
View Journal | View Issue

Check for updates

Cite this: *J. Mater. Chem. C*, 2023, **11**, 2229

High-power piezoelectric behavior of acceptor-doped ⟨001⟩ and ⟨111⟩ textured piezoelectric ceramics†

Haoyang Leng,[a] Yongke Yan,[a] Xiaotian Li,[a] Sumanta Kumar Karan,[a] Mark Fanton[b] and Shashank Priya*[a]

Piezoelectric ceramics with high piezoelectric co-efficient, d_{33}, and mechanical quality factor, Q_m, are required in high-power applications. ⟨001⟩ and ⟨111⟩ textured $Pb(In_{1/2}Nb_{1/2})O_3$–$Pb(Mg_{1/3}Nb_{2/3})O_3$–$PbTiO_3$ ceramics were fabricated using templated grain growth method and their high-power electromechanical properties were characterized. It is shown that ⟨001⟩ textured ceramics possess higher d_{33} compared to random and ⟨111⟩ textured counterparts, while the Q_m is strongly enhanced in ⟨111⟩ textured ceramics due to less favored polarization rotation. MnO_2 doping is shown to further improve the Q_m values for both ⟨001⟩ and ⟨111⟩ textured ceramics because of the restricted polarization switching induced by the defect dipole. Doped ⟨001⟩ textured ceramics can exhibit the high d_{33} and moderate Q_m (d_{33} = 725 pC N^{-1}, Q_m = 716) in comparison with ⟨111⟩ textured ceramics exhibiting low d_{33} and high Q_m (d_{33} = 350 pC N^{-1}, Q_m = 1495). Owing to the combinatory soft and hard piezoelectric properties, the doped ⟨001⟩ textured ceramics exhibit 1.5× higher vibration velocity (∼0.90 m s^{-1}) in comparison with commercial hard PZTs. Interestingly, a slightly higher vibration velocity (∼0.94 m s^{-1}) can be obtained in doped ⟨111⟩ textured ceramics, which is mainly attributed to the high Q_m and low elastic compliance s_{11}. These results demonstrate the promise of textured piezoelectric ceramics for high-power applications.

Received 8th September 2022,
Accepted 27th November 2022

DOI: 10.1039/d2tc03786f

rsc.li/materials-c

1. Introduction

The lead-free piezoelectric materials have been extensively investigated due to their environmental safety benefits. However, compared to lead-based piezoelectric materials, the lead-free piezoelectric materials have inferior comprehensive properties, limiting their practical applications.[1,2] Lead-based relaxor-PT materials, such as $Pb(Mg_{1/3}Nb_{2/3})O_3$–$PbTiO_3$ (PMN–PT), are promising candidates for electromechanical devices including actuators, transducers, and sensors, due to their superior piezoelectric properties in comparison to conventional PZT ceramics.[3–5] However, the low phase transition temperatures in PMN–PT, including Curie temperature T_c and rhombohedral to tetragonal phase transition temperature T_{r-t}, limit the temperature stability.[6,7] The relaxor ternary system, $Pb(In_{1/2}Nb_{1/2})O_3$–$Pb(Mg_{1/3}Nb_{2/3})O_3$–$PbTiO_3$ (PIN–PMN–PT), can exhibit higher phase transition temperatures while retaining comparable piezoelectric properties to that of PMN–PT.[8–10]

For high-power transducer applications, piezoelectric ceramics need to possess high piezoelectric coefficient d and mechanical quality factor Q_m in order to maximize vibration velocity ($v_{rms} \propto Q_m \cdot d$) and output power ($P \propto v^2$).[11–13] Prior studies have shown that the piezoelectric constant d_{33} of PIN–PMN–PT can be significantly improved by texturing along ⟨001⟩ crystallographic direction using template grain growth (TGG) method. For example, the ⟨001⟩ textured PIN–PMN–PT ceramics can exhibit a high d_{33} of 927 pC N^{-1}, which is ∼2× higher than that of non-textured (random) counterparts.[9] The enhanced d_{33} of ⟨001⟩ textured ceramics can be explained by invoking the piezoelectric anisotropy similar to that shown for piezoelectric single crystals.[14,15] However, the textured PIN–PMN–PT ceramics possess a low Q_m (∼100), which restricts their applications in high-power transducer devices.[16] Similar to MnO_2 doped PIN–PMN–PT single crystal, acceptor doping can be an effective way to improve the Q_m value of textured PIN–PMN–PT ceramics. In these cases, the acceptor ions substitute on the B-site of the perovskite structure, creating defect dipoles consisting of negatively charged center defect ions paired with positively charged oxygen vacancies.[17–19] These defect dipoles pin the domain wall motion under applied

---

[a] *Department of Materials Science and Engineering, and Materials Research Institute, The Pennsylvania State University, University Park, Pennsylvania 16802, USA. E-mail: sup103@psu.edu*

[b] *Applied Research Laboratory, The Pennsylvania State University, University Park, PA, 16801, USA*

† Electronic supplementary information (ESI) available. See DOI: **https://doi.org/10.1039/d2tc03786f**

electric field, leading to reduced mechanical loss and enhanced Q_m in piezoelectric ceramics. Prior results show that ⟨001⟩ textured MnO_2-doped 0.24PIN–0.42PMN–0.34PT piezoelectric ceramics can exhibit an excellent combination of d_{33} and Q_m (d_{33} = 725 pC N^{-1}, Q_m = 716).[20] However, the effect of MnO_2 doping on Q_m value in polycrystalline ceramics for different crystallographic orientations is not well understood. One of the reasons for this lack of understanding is the difficulty in synthesizing ⟨111⟩ textured PIN–PMN–PT ceramics as compared to ⟨001⟩ orientation. Here, we address this issue and provide synthesis pathway to consistently realize ⟨111⟩ oriented piezoelectric ceramics and use this success in synthesis to provide comprehensive comparative analysis of ⟨001⟩ and ⟨111⟩ oriented PIN–PMN–PT ceramics.

We have investigated the effect of ⟨001⟩ and ⟨111⟩ texturing on piezoelectric properties and mechanical quality factor of undoped and MnO_2-doped 0.24PIN–0.42PMN–0.34PT ceramics to understand the orientation dependence. Two different types of templates, ⟨001⟩ and ⟨111⟩ $BaTiO_3$ (BT) crystals were used to texture 0.24PIN–0.42PMN–0.34PT ceramics along ⟨001⟩ and ⟨111⟩ directions, respectively. The piezoelectric properties and mechanical quality factor of random, ⟨001⟩ oriented, and ⟨111⟩ oriented ceramics were measured and compared to understand the differences in their magnitudes as well as influence of MnO_2 doping. High-power piezoelectric vibration characteristics were measured for both doped ⟨001⟩ and ⟨111⟩ textured ceramics to evaluate their promise for practical applications.

2. Experimental procedure

The compositions described by the formulation, $0.24Pb(In_{1/2}Nb_{1/2})O_3$–$0.42Pb(Mg_{1/3}Nb_{2/3})O_3$–$0.34PbTiO_3$ (0.24PIN–0.42PMN–0.34PT) and 2 mol% MnO_2-doped 0.24PIN–0.42PMN–0.34PT, were synthesized using two-step columbite precursor method.[17] The ⟨001⟩ and ⟨111⟩ $BaTiO_3$ (BT) templates were prepared by topochemical microcrystal conversion (TMC) method.[21,22] The ceramic slurry for tape-casting was prepared by ball-milling the 0.24PIN–0.42PMN–0.34PT or 2 mol% MnO_2-doped 0.24PIN–0.42PMN–0.34PT matrix powders with polyvinyl butyral (PVB) binder, toluene solvent and 0.25 wt% CuO. In this ceramic slurry, 2 vol% ⟨001⟩ and ⟨111⟩ BT templates were mixed by magnetic stirring and the mixture was tape casted at a rate of 20 mm s^{-1} using a doctor blade with height of 0.25 mm. The dried green tapes were cut, stacked, and laminated at 85 °C under 20 MPa pressure for 15 min. The green samples were heated to 600 °C with a heating rate of 0.5 °C min^{-1} and fired for 1h to remove the organic binder, and then cold-isostatically pressed at 200 MPa for 1 min. The 0.24PIN–0.42PMN–0.34PT with 0 vol% BT (random), 0.24PIN–0.42PMN–0.34PT with 2 vol% ⟨001⟩ BT (⟨001⟩ textured), and 0.24PIN–0.42PMN–0.34PT with 2 vol% ⟨111⟩ BT (⟨111⟩ textured) samples were subsequently embedded in calcined 0.24PIN–0.42PMN–0.34PT powders with 1.5 wt% excess PbO and sintered at 1220 °C for 6 h in air. The 2 mol% MnO_2-doped 0.24PIN–0.42PMN–0.34PT with 2 vol% ⟨001⟩ BT (doped-⟨001⟩ textured) and 2 mol% MnO_2-doped 0.24PIN–0.42PMN–0.34PT with 2 vol% ⟨111⟩ BT (doped-⟨111⟩ textured) samples were embedded in calcined 2 mol% MnO_2-doped 0.24PIN–0.42PMN–0.34PT powders with 1.5 wt% excess PbO and sintered at 1200 °C for 6 h in air. The sintered samples were polished to remove residual powders. The sintered densities were measured by Archimedes' method, as listed in Table S1 (ESI†).

The phases and microstructures were determined using X-ray diffraction (XRD, PANalytical Empyrean) and field-emission scanning electron microscopy (FESEM Apreo) in combination with electron backscatter diffraction (EBSD), respectively. The ⟨001⟩ and ⟨111⟩ texture degree F was evaluated by Lotgering factor method according to the X-ray diffraction patterns in the 2-theta range of 20–60°.[23,24] The piezoelectric coefficient d_{33} was measured by using a quasi-static d_{33} meter (YE2730A, APC Products). The dielectric permittivity ε_r as a function of temperature was measured at 1 kHz by a multifrequency LCR meter (HP4284A). Ferroelectric P–E hysteresis loops and the piezoelectric unipolar strains were measured at 1 Hz using a Precision Premier II ferroelectric Tester (Radiant Technologies). The mechanical coupling coefficient k and mechanical quality factor Q_m were determined by resonance and anti-resonance technique using impedance analyzer (Keysight E4990A). Piezoresponse force microscopy (PFM) mode in Bruker Icon II instrument was used to characterize the domain structure and microscopic piezoresponse. The high-power piezoelectric vibration characteristics of commercial hard PZT (APC 841) sample, and ⟨001⟩ and ⟨111⟩ textured ceramics were measured in the transverse 31 mode using a laser vibrometer (PSV-500 by Polytec).

3. Results and discussion

3.1. Fabrication of ⟨001⟩ and ⟨111⟩-textured ceramics

Fig. 1a shows X-ray diffraction (XRD) patterns for ⟨001⟩ and ⟨111⟩ oriented BT templates after the topochemical conversion reaction. It can be found that both ⟨001⟩ and ⟨111⟩ oriented BT templates exhibit tetragonal perovskite phase. The scanning electron microscopy (SEM) images of ⟨001⟩ and ⟨111⟩ BT templates are shown in Fig. 1d. Both ⟨001⟩ and ⟨111⟩ BT templates possess high-aspect ratio plate-like morphologies. The length and thickness of ⟨001⟩ BT templates are in the ranges of 5–10 μm and 0.2–1.2 μm, respectively, while the ⟨111⟩ BT templates have a larger size with 20–30 μm in length and 1.5–3 μm in thickness. Fig. 1b shows the schematic illustration of Ba^{2+} and O^{2-} ions arrangement along ⟨001⟩ and ⟨111⟩ directions for BT templates, which demonstrates that ⟨111⟩ BT has higher atomic packing density compared to ⟨001⟩ BT. The XRD patterns of random and textured ceramics are shown in Fig. 1c. All samples exhibit perovskite phase, while the ⟨001⟩ and ⟨111⟩ textured ceramics exhibit enhanced intensities of (00l) and (111) diffraction peaks, respectively, in comparison with random counterpart, indicating the strong ⟨001⟩ or ⟨111⟩ orientation of grains. The calculated Lotgering factors F_{00l} and F_{111} for ⟨001⟩ and ⟨111⟩ textured ceramics are 81.7% and 66%, respectively. After MnO_2 doping, both doped ⟨001⟩ and ⟨111⟩ textured ceramics can exhibit much higher F_{00l} of 98% and F_{111} of 85%, respectively, indicating that the MnO_2 dopant can effectively promote the ⟨001⟩ or ⟨111⟩ texture development in

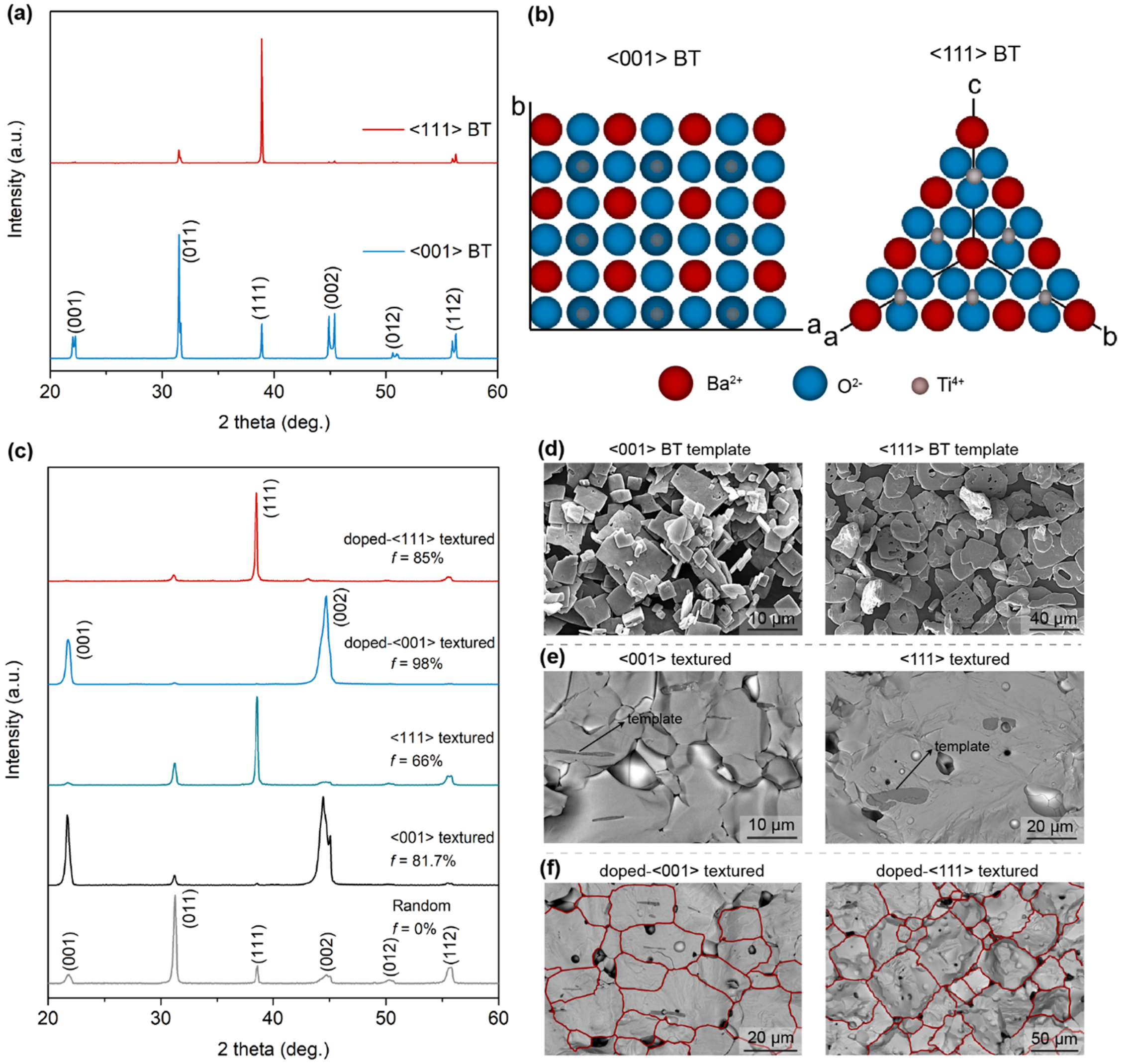

Fig. 1 (a) XRD patterns and (b) schematic diagrams of ion arrangement for ⟨001⟩ and ⟨111⟩ oriented BT templates. (c) XRD patterns of PIN–PMN–PT with 0 vol% BT (random), PIN–PMN–PT with 2 vol% ⟨001⟩ oriented BT (abbreviated as ⟨001⟩ textured), PIN–PMN–PT with 2 vol% ⟨111⟩ oriented BT (⟨111⟩ textured), 2 mol% MnO_2-doped PIN–PMN–PT with 2 vol% ⟨001⟩ oriented BT (doped-⟨001⟩ textured), and 2 mol% MnO_2-doped PIN–PMN–PT with 2 vol% ⟨111⟩ oriented BT (doped-⟨111⟩ textured) ceramics. (d) SEM images of ⟨001⟩ and ⟨111⟩ oriented BT templates. (e) Cross-sectional SEM images of ⟨001⟩ and ⟨111⟩ textured ceramics. (f) Cross-sectional SEM image of doped-⟨001⟩ and ⟨111⟩ textured ceramics (The visible grain boundaries are marked by red lines).

PIN–PMN–PT ceramics. Fig. 1e and f show the cross-sectional SEM images for undoped and doped ⟨001⟩ and ⟨111⟩ textured ceramics, respectively. The epitaxial grain growth of PIN–PMN–PT matrix on ⟨001⟩ and ⟨111⟩ BT templates (black areas) can be observed in this figure. In addition, it can be found that the doped ⟨001⟩ and ⟨111⟩ textured ceramics can exhibit textured microstructures with dense grain structure. The enhanced grain growth induced by MnO_2-doping has also been found in PZT–PZN piezoelectric ceramics, which is assumed to be caused by diffusion of oxygen vacancies.[25] The oxygen vacancies induced by MnO_2-doping can facilitate the lattice diffusion, leading to the enhanced grain growth.[20,25] Considering the different sizes of ⟨001⟩ and ⟨111⟩ BT templates, it is worth noting that there is still space to further improve the ⟨111⟩ texturing degree of PIN–PMN–PT ceramics by optimizing the tape-casting parameters (*e.g.* blade gap height and tape-casting speed). This presents opportunities for future studies.

Fig. 2 compares the grain growth behavior of ⟨001⟩ and ⟨111⟩ oriented PIN–PMN–PT matrix grains. The EDS maps indicate the excellent stability of ⟨001⟩ and ⟨111⟩ BT templates inside the PIN–PMN–PT matrix during the template grain growth process at high temperatures. It is interesting to note that ⟨001⟩ and ⟨111⟩ oriented grains exhibit different shapes. Specifically, the ⟨001⟩ oriented PIN–PMN–PT grains grown from the ⟨001⟩ BT template exhibit a rectangular cross-section, while the ⟨111⟩ oriented counterparts display a diamond shape cross-section (Fig. 2a and b). The different grain morphologies in doped-⟨001⟩ and ⟨111⟩ textured ceramics can also be observed in Fig. 1f. Fig. 2c shows the schematic diagrams describing the different grain growth behavior of ⟨001⟩ and ⟨111⟩ oriented grains. For the

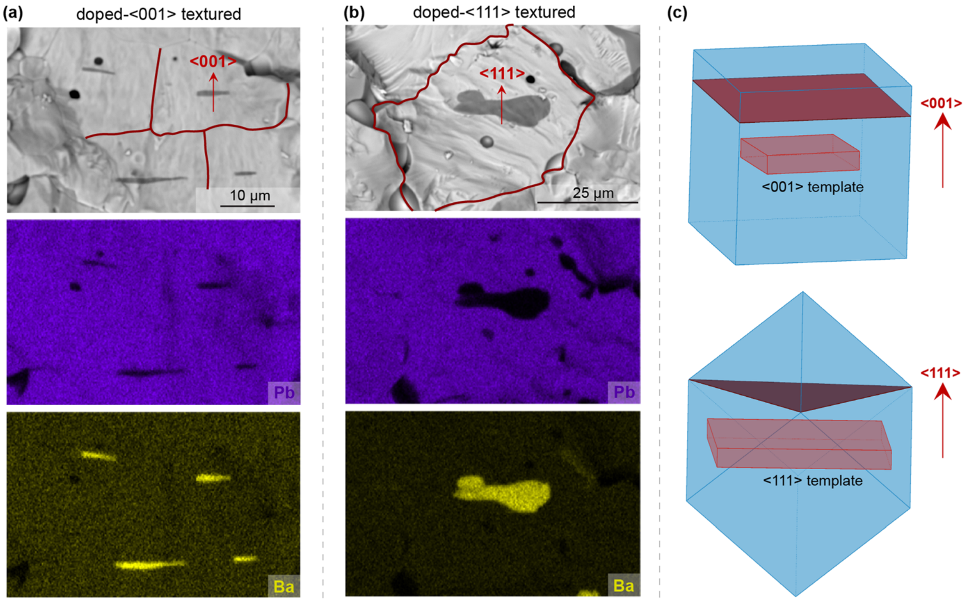

Fig. 2 (a) and (b) Cross-sectional SEM images and the corresponding EDS element mapping of doped-⟨001⟩ and ⟨111⟩ textured ceramics. (c) Schematic diagrams of ⟨001⟩ and ⟨111⟩ oriented grain growth of PIN–PMN–PT matrix on ⟨001⟩ and ⟨111⟩ BT templates.

grains grown on the surface of ⟨001⟩ template, they will follow a layer-by-layer growth mode to form {001}-faced cuboids. This is due to the fact that the perovskite phase have the lowest energy along {001} surface and the ⟨001⟩ template has plate-like morphologies.[21,26] Compared to the ⟨001⟩ oriented grains, the ⟨111⟩ oriented grains grown on the surface of ⟨111⟩ template will grow fastest along ⟨111⟩ direction due to the high surface energy of {111} planes, leading to the absence of {111} surfaces in the final shape and forming triangular bi-pyramids with low-energy density {001} surfaces.

The SEM images of polished surface and the corresponding EBSD images for random and textured ceramics are shown in Fig. 3. The doped ⟨111⟩ textured ceramics possess much larger grain size compared to doped ⟨001⟩ textured ceramics. As shown in Fig. 1d, the ⟨111⟩ BT templates have much larger crystal size compared to ⟨001⟩ BT templates. Since the total BT

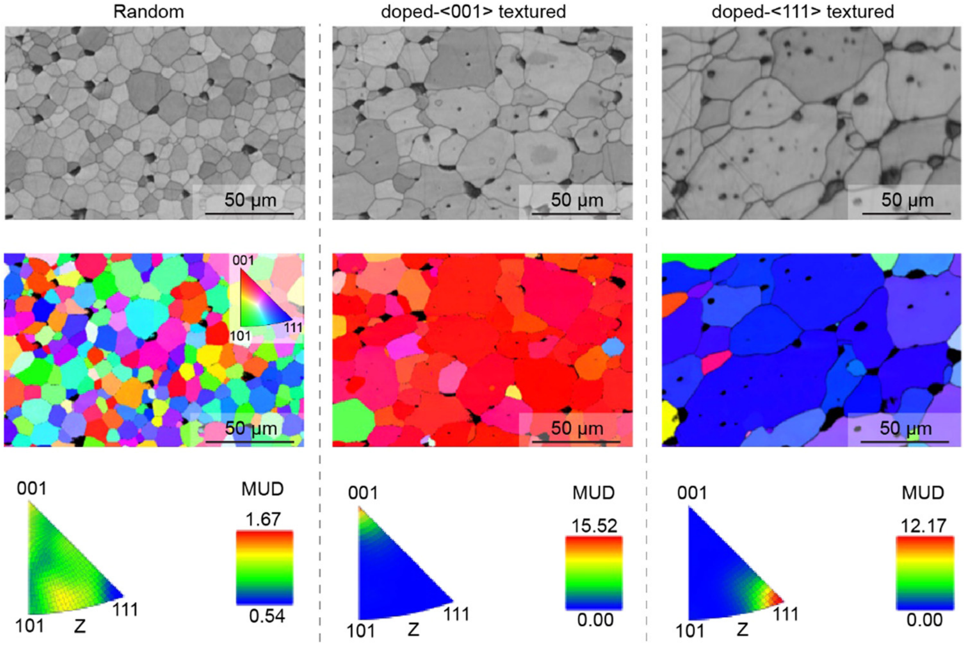

Fig. 3 SEM images of polished surface and the corresponding EBSD images of random, doped-⟨001⟩ and ⟨111⟩ textured ceramics. In EBSD, MUD (multiple of uniform density) is a parameter used for the statistical description of the intensity of texture. MUD value of 1 indicates randomly oriented gains and MUD value significantly >1 indicates textured grains.

template content inside the PIN–PMN–PT matrix is fixed for ⟨001⟩ and ⟨111⟩ textured ceramics, ⟨111⟩ textured ceramics will have lower number of the templates (f_T) inside the PIN–PMN–PT matrix compared to ⟨001⟩ textured ceramics. As a result, ⟨111⟩ oriented grains have longer crystal growth length (x_T) before impinging on surrounding textured grains, based on the relationship $x_T = \left(\frac{6}{\pi f_T}\right)^{\frac{1}{3}}$,[27] leading to the larger grain sizes. The EBSD mapping further provides the evidence for strong ⟨001⟩ and ⟨111⟩ orientation of grains in textured ceramics.

3.2. Dielectric and piezoelectric properties of ⟨001⟩ and ⟨111⟩-textured ceramics

Fig. 4a shows the dielectric constant as a function of temperature for random, ⟨001⟩ textured, and ⟨111⟩ textured ceramics. First, two dielectric peaks at approximately 118 °C and 219 °C, corresponding to rhombohedral to tetragonal (T_{r-t}) and tetragonal to cubic (T_c) phase transitions can be found in random ceramic. Both ⟨001⟩ and ⟨111⟩ textured ceramics have T_c value around 219 °C, indicating that the presence of 2 vol% BT template has little influence on the transition temperature. After MnO_2 doping, the Curie temperature T_c slightly decreases to 204 °C for doped ⟨001⟩ and ⟨111⟩ textured ceramics. Similar phenomenon induced by Mn doping has also been reported in PSZTN system.[28] Fig. 4b compares the unipolar strain response measured at the electric field of 30 kV cm^{-1} for random, ⟨001⟩ textured, and ⟨111⟩ textured ceramics. The strain values follow the trend, $S_{\langle 001 \rangle} > S_{\text{Random}} > S_{\langle 111 \rangle}$ at 30 kV cm^{-1}, which is consistent with the trend of measured small signal d_{33} values for random and textured ceramics in Table 1. From the P–E hysteresis loops shown in Fig. 4c, it is interesting to note that both MnO_2-doped ⟨001⟩ and ⟨111⟩ textured ceramics possess higher remnant polarization (P_r) compared to undoped ⟨001⟩ and ⟨111⟩ counterparts. The lower P_r values of undoped ⟨001⟩ and ⟨111⟩ textured ceramics can be understood from the impedance spectra shown in Fig. 4d. It is known that the maximum impedance phase angle θ_Z in impedance spectra is related to the poling degree of piezoelectric ceramics.[29,30] The undoped ⟨001⟩ and ⟨111⟩ textured ceramics exhibit lower θ_Z values of 75° and 72°, respectively, compared to doped ⟨001⟩ and ⟨111⟩ textured counterparts with high θ_Z values of 89° and 88°, respectively, indicating the low poling degree of undoped textured ceramics. The low poling degree implies insufficient polarization switching under electric field, resulting in low P_r value of piezoelectric ceramics. In addition to the different polarization values, the apparent horizontal shift in the P–E hysteresis loops of MnO_2-doped textured ceramics can be observed in comparison with undoped textured counterparts (Fig. 4c), suggesting the existence of internal bias field E_i induced by the well oriented defect dipoles. The E_i value can be calculated by the equation $E_i = (E_{c+} + E_{c-})/2$, where E_{c+} and E_{c-} are the intersections of P–E hysteresis loops with the positive and negative E field axis, respectively.[31] The E_i value is calculated to be 1.10 kV cm^{-1} and 1.31 kV cm^{-1} for doped ⟨001⟩ and ⟨111⟩ textured ceramics, respectively.

The detailed dielectric and piezoelectric properties of random, ⟨001⟩ textured, and ⟨111⟩ textured ceramics can be found

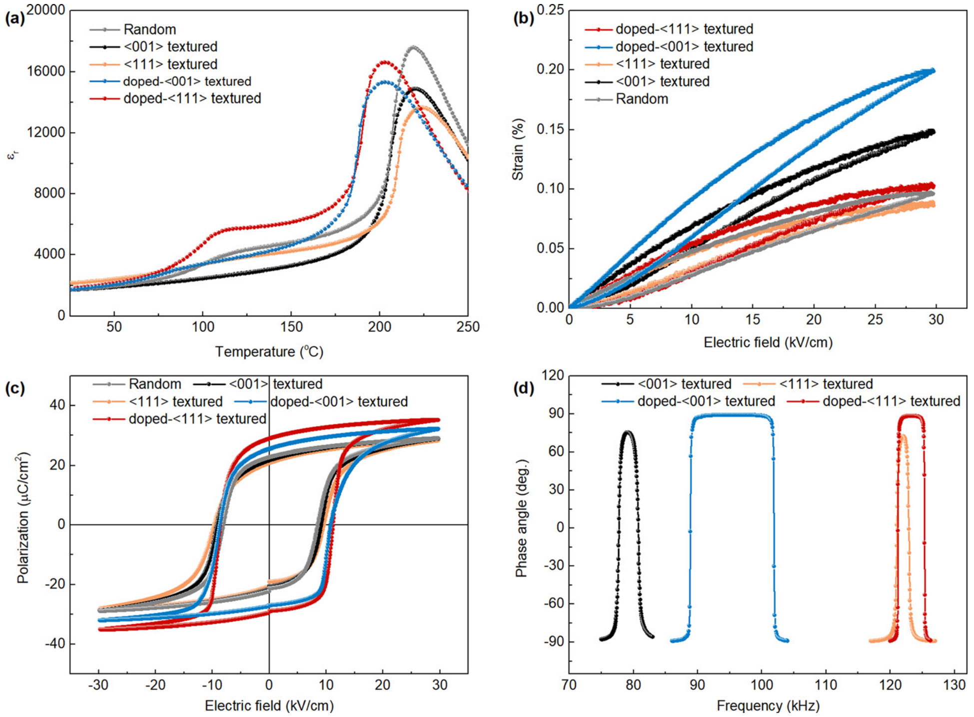

Fig. 4 (a) Dielectric permittivity (measured at 1 kHz) and (b) unipolar S–E curves (measured at 1 Hz) for random, ⟨001⟩ and ⟨111⟩ textured, and doped ⟨001⟩ and ⟨111⟩ textured ceramics. (c) P–E hysteresis loops (measured at 1 Hz) and (d) phase angle spectra (measured with the voltage amplitude of 500 mV) for random, ⟨001⟩ and ⟨111⟩ textured, and doped ⟨001⟩ and ⟨111⟩ textured ceramics.

Table 1 Dielectric and piezoelectric properties for both random, ⟨001⟩ and ⟨111⟩ textured piezoelectric ceramics

Specimen	Template	F_{001} [%]	$\varepsilon_{33}{}^{T}/\varepsilon_o$	s_{11} [μm^2 N^{-1}]	tan δ [%]	d_{33} [pC N^{-1}]	d_{31} [pC N^{-1}]	k_{31}	Q_m
Random[a]	0	0	1836	12.39	0.96	304	101	0.22	147
⟨001⟩ textured	2 vol% ⟨001⟩ BT	81.7	1727	14.44	0.9	412	138	0.29	165
⟨111⟩ textured	2 vol% ⟨111⟩ BT	66	2097	11.20	0.7	274	82	0.18	385
Doped-⟨001⟩ textured[a]	2 vol% ⟨001⟩ BT	98	1498	15.90	0.42	725	247	0.54	716
Doped-⟨111⟩ textured	2 vol% ⟨111⟩ BT	85	1850	9.90	0.5	350	116	0.29	1495
Commercial APC 841	0	0	1152	11.24	0.5	312	108	0.33	1050

[a] Ref. 20.

in Table 1. The piezoelectric coefficient d_{33} of ⟨001⟩ textured ceramics is higher than that of random ceramics, while the ⟨111⟩ textured ceramics show the lowest d_{33} value.

For perovskite ferroelectrics, the piezoelectric coefficient d_{33} is proportional to $Q_{33}P_S\varepsilon_{33}$.[32–34] The electrostrictive coefficient Q_{33} of perovskite ferroelectrics exhibits orientation dependent behavior. The maximum Q_{33} is along the ⟨001⟩ direction, while the minimum value is along the ⟨111⟩ direction.[34] In addition, the anisotropy of Q_{33} is not sensitive to the ferroelectric phases. As a result, the ⟨001⟩ textured ceramics will exhibit the highest d_{33} value compared to random and ⟨111⟩ textured ceramics. Although the highest d_{33} value can be obtained in ⟨001⟩ textured ceramics, the percentage enhancement in d_{33} coming from the ⟨001⟩ texturing is less than 40% (from 304 pC N^{-1} in random ceramics to 412 pC N^{-1} in ⟨001⟩ textured ceramics) due to the incomplete template grain growth of ⟨001⟩ textured ceramics ($F_{001} \sim 81.7\%$).

As shown in Table 1, the ⟨111⟩ textured ceramics possess much higher mechanical quality factor Q_m of 385 in comparison with ⟨001⟩ textured ceramics exhibiting Q_m value of 165, indicating the orientation dependence of Q_m in PIN–PMN–PT ceramics. This is different from the softening and hardening effects induced by dopants in piezoelectric ceramics. It is known that the polarization rotation under external electric field will result in high magnitude of mechanical loss (tan γ) in ferroelectrics.[35,36] When an electric field is applied to poled piezoelectric sample with multi-domain configuration, the torque per unit volume for the polarization rotation can be expressed as:[37]

$$M = \frac{q\vec{E} \times \vec{l}}{V} = \frac{qEl \sin\varphi}{V} = \left(\frac{ql}{V}\right) \cdot E \cdot \sin\varphi = PE \sin\varphi \qquad (1)$$

where q represents the charge of polarization P, l is the effective distance between the negative charge and positive charge point, V is the unit cell volume, and φ is the angle between the polarization P and external electric field E. It can be found that a larger angle φ will favor the polarization rotation under the external electric field, leading to the high mechanical loss (low Q_m). As shown in Fig. S1 (ESI†), the φ value is around 54.7° and 0° for ⟨001⟩ and ⟨111⟩ oriented samples, respectively. This implies that the ⟨111⟩ oriented samples will possess lower mechanical loss (high Q_m) compared to ⟨001⟩ oriented counterparts, which is consistent with our experimental results.

After MnO_2 doping, the d_{33} of ⟨001⟩ textured ceramics exhibit significant improvement from 412 pC N^{-1} to 725 pC N^{-1}, which is due to the improved ⟨001⟩ texturing degree (F_{001} value from 81.7% to 98%) and poling degree (θ_Z value from 75° to 89°) induced by MnO_2 doping effect. The ⟨111⟩ textured ceramics also exhibit similar trend, where the d_{33} value increases from 274 pC N^{-1} to 350 pC N^{-1} due to the improved poling degree (θ_Z value from 72° to 88°). The low poling degree of piezoelectric ceramics is usually caused by different losses, including mechanical loss tan γ, dielectric loss tan δ, and piezoelectric loss tan θ.[37–39] These three losses can be obtained by simulating the impedance spectra using the loss incorporated equivalent circuit.[39,40] As shown in Fig. 5a–d, the simulation results demonstrate that both ⟨001⟩ and ⟨111⟩ textured ceramics possess much higher loss in comparison with doped ⟨001⟩ and ⟨111⟩ textured counterparts. The simulation results in Fig. 5e–g and Fig. S2 (ESI†) show the effect of different magnitudes and different types of loss on phase angle θ_Z of ⟨001⟩ and ⟨111⟩ textured ceramics, respectively. It was found that both dielectric loss tan δ, and piezoelectric loss tan θ have minimal effect on phase angle θ_Z, while mechanical loss tan $\gamma = 1/Q_m$ shows the significant effect on θ_Z in both ⟨001⟩ and ⟨111⟩ textured ceramics. A lower mechanical loss tan γ (high Q_m) will lead to higher phase angle θ_Z, which is consistent with our experimental results where doped textured ceramics show higher θ_Z value than undoped counterparts due to the reduced mechanical loss tan γ (high Q_m). The doped ⟨001⟩ textured ceramics still exhibits much higher piezoelectric response d_{33} in comparison with doped ⟨111⟩ textured counterparts due to the orientation dependent behavior of d_{33} as discussed before.

In addition to the intrinsic contribution from the piezoelectric anisotropy, it is known that the domain size and morphology can strongly affect the piezoelectric properties.[41–43] Thus, piezoresponse force microscopy (PFM) was applied to observe the domain structures for both doped ⟨001⟩ and ⟨111⟩ textured ceramics. As shown in Fig. 6a and b, both doped ⟨001⟩ and ⟨111⟩ textured ceramics have an island-type domain structure, while the doped ⟨001⟩ textured ceramic exhibits a smaller and homogeneous domain than that of doped ⟨111⟩ textured counterpart. The domain size D is proportional to the domain wall energy γ based on the relationship $D \propto \sqrt{\gamma}$.[44] The smaller domains with reduced domain wall energy in doped ⟨001⟩ textured ceramic can facilitate the domain wall motion and domain switching under the external electric field, leading to the enhanced extrinsic piezoelectric contributions. Thus, the domain size may be a factor responsible for the high piezoelectric response of doped ⟨001⟩ textured ceramic. Previous domain size studies on $Pb(Zr,Ti)O_3$ and $BaTiO_3$ systems find that the domain size increases with increasing grain size.[45] We also observe the similar grain-domain size relation in textured

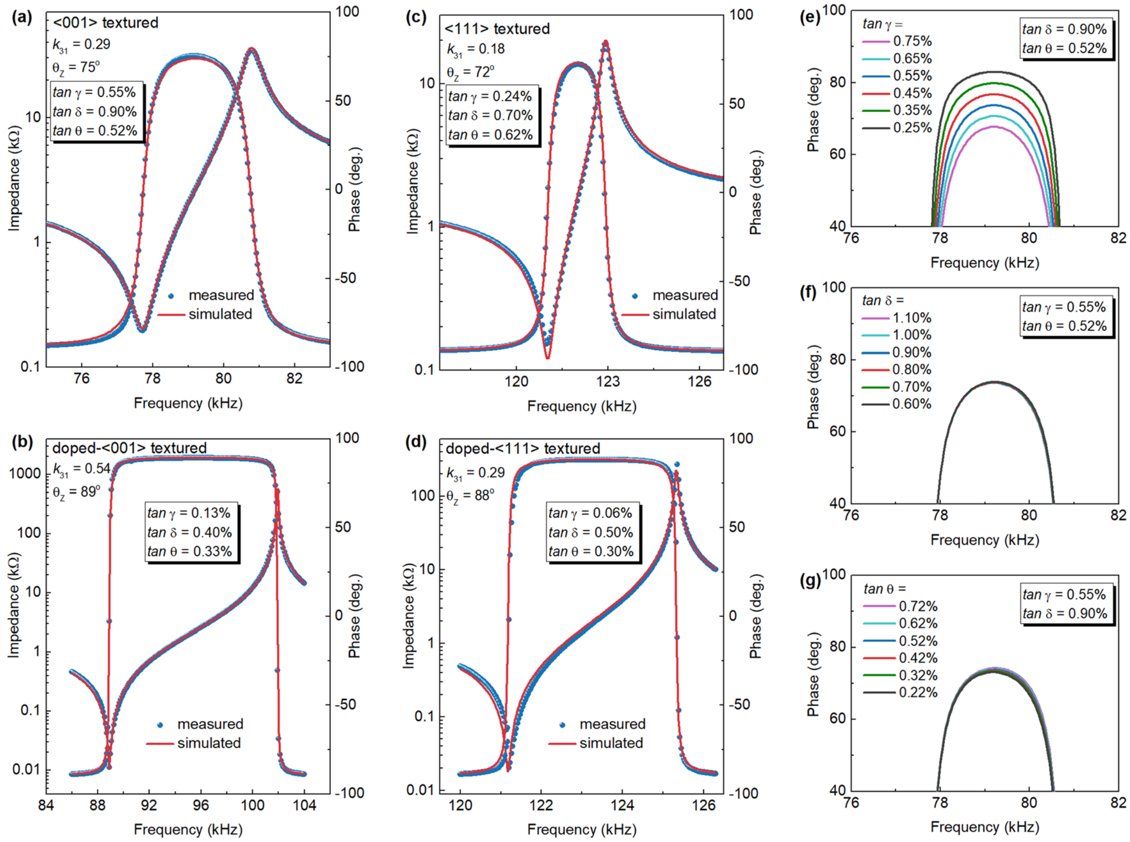

Fig. 5 Impedance and phase angle spectra for (a) ⟨001⟩ textured and (b) doped-⟨001⟩ textured ceramics. Impedance and phase angle spectra for (c) ⟨111⟩ textured and (d) doped-⟨111⟩ textured ceramics (the mechanical loss tan γ, dielectric loss tan δ, and piezoelectric loss tan θ were fitted using loss incorporated equivalent circuit). (e)–(g) Simulated phase angle spectra for ⟨001⟩ textured ceramic with different loss factors.

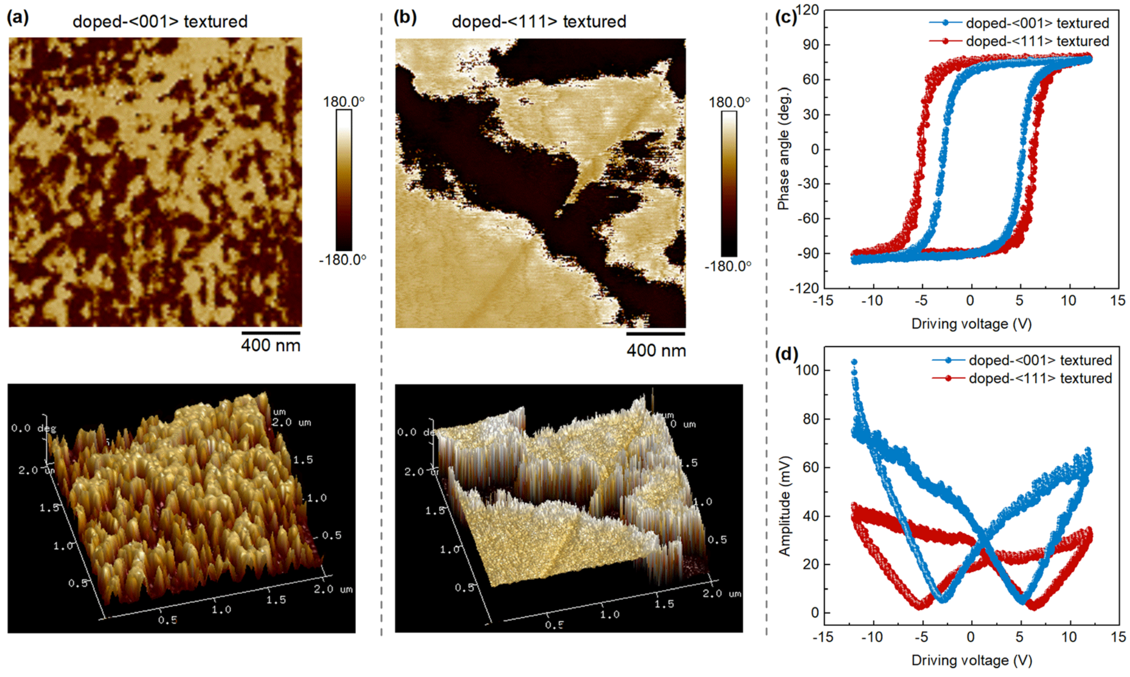

Fig. 6 (a) and (b) 2D and 3D PFM phase images of domain structure for doped-⟨001⟩ and ⟨111⟩ textured ceramics. (c) Microscopic piezoresponse hysteresis loops and (d) butterfly-shaped amplitude *versus* driving voltage curves for doped-⟨001⟩ and ⟨111⟩ textured ceramics.

ceramics where doped ⟨111⟩ textured ceramics with larger grain size can exhibit larger domain size in comparison with doped ⟨001⟩ textured counterparts. In addition, it has been reported that the strain induced by the template-matrix interface in textured ceramics constrains the domain size, leading to the fine domain structure.[24,46] Based on SEM results, the ⟨111⟩ BT templates have lower frequency inside the PIN–PMN–PT matrix than ⟨001⟩ BT templates. Thus, the strain effect on domain structure induced by the template-matrix interface is smaller in doped ⟨111⟩ textured ceramics compared to doped ⟨001⟩ textured ceramics.

To further understand the effect of crystallographic orientation on microscopic piezoresponse, both phase-voltage hysteresis loops and amplitude-voltage butterfly curves were measured at local positions in ⟨001⟩ and ⟨111⟩ textured grains by applying a sequence of DC voltage from −12 V to 12 V with a superimposed AC signal of 5V to the PFM tip (Fig. 6c and d). The phase hysteresis loops exhibit nearly 180° phase reversal, indicating the sufficient polarization switching of doped ⟨001⟩ and ⟨111⟩ textured ceramics. However, the average amplitude of piezoresponse in doped ⟨001⟩ textured ceramic is much higher than that of doped ⟨111⟩ textured ceramic (Fig. 6d), which is consistent with the trend of measured macroscopic piezoresponse for doped ⟨001⟩ and ⟨111⟩ textured ceramics.

3.3. Crystallographic orientation dependence of high-power properties

The mechanical quality factor for doped textured ceramics also exhibits anisotropic behavior, where the ⟨111⟩ textured ceramics possess much higher Q_m value of 1495 in comparison with doped ⟨001⟩ textured ceramics exhibiting Q_m value of 716 (Table 1). As shown in Table 1, the enhancement of Q_m after $\mathrm{MnO_2}$ doping can be found in both ⟨001⟩ and ⟨111⟩ textured ceramics. For $\mathrm{MnO_2}$-doped piezoelectric ceramics, acceptor ions like Mn^{2+} or Mn^{3+} will substitute on B-site of perovskite structure, replacing higher valent Ti^{4+} and Nb^{5+} due to the similar ionic radius, resulting in the formation of defect dipoles consisting of negatively charged acceptor ions and positively charged oxygen vacancies, $\mathrm{Mn}_{\mathrm{Ti}}'' - \mathrm{V}_{\mathrm{O}}^{\bullet\bullet}$.[28,35] The formation of defect dipoles in $\mathrm{MnO_2}$-doped textured ceramics can restrain the oxygen vacancy $\mathrm{V}_{\mathrm{O}}^{\bullet\bullet}$ migration (higher activation energy E_a of the conduction) and decrease in the electrical conductivity, as shown in Fig. 7, leading to the lower dielectric loss tan δ in doped ⟨001⟩ and ⟨111⟩ textured ceramics (Table 1).

On the other hand, the $\mathrm{Mn}^{2+} - \mathrm{V}_{\mathrm{O}}^{\bullet\bullet}$ defect dipoles will induce defect polarization P_D, which can be represented by:

$$P_D = \frac{\sum p_D}{V} = \frac{c p_D}{V} \tag{2}$$

where p_D is the defect dipole moment of $\mathrm{Mn}_{\mathrm{Ti}}'' - \mathrm{V}_{\mathrm{O}}^{\bullet\bullet}$ and V is the lattice volume. The defect polarization P_D will prefer to align in the same direction of spontaneous polarization P_S based on the symmetry conforming short-range ordering (SC-SRO).[47,48] When an external electric field E is applied to the sample, the spontaneous polarization P_S prefers to switch to the same direction of E, while the defect dipole induced polarization P_D will remain along its original direction since the P_D switching requires $\mathrm{V}_{\mathrm{O}}^{\bullet\bullet}$ diffusion, and the polarization switching under electric field is diffusion-less process.[17] The P_D will then generate a restoring force to constrain the P_S switching under electric field, as shown in Fig. 8a. To further confirm the constrained P_S switching in $\mathrm{MnO_2}$-doped textured ceramics, the activation energy E_a for polarization switching for both undoped and $\mathrm{MnO_2}$-doped textured ceramics is calculated and compared. For piezoelectric ceramics, the back-switching polarization P_{bc} will increase with

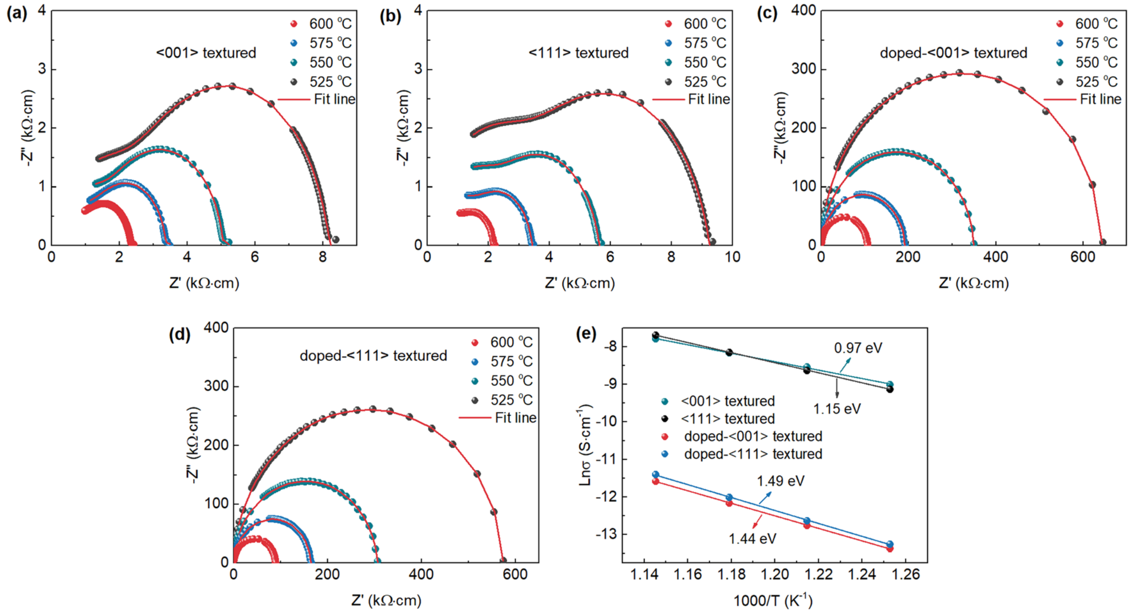

Fig. 7 (a)–(d) Temperature dependent complex impedance spectra and (e) corresponding Arrhenius plots of ionic conductivities for ⟨001⟩ and ⟨111⟩ textured, and doped ⟨001⟩ and ⟨111⟩ textured ceramics.

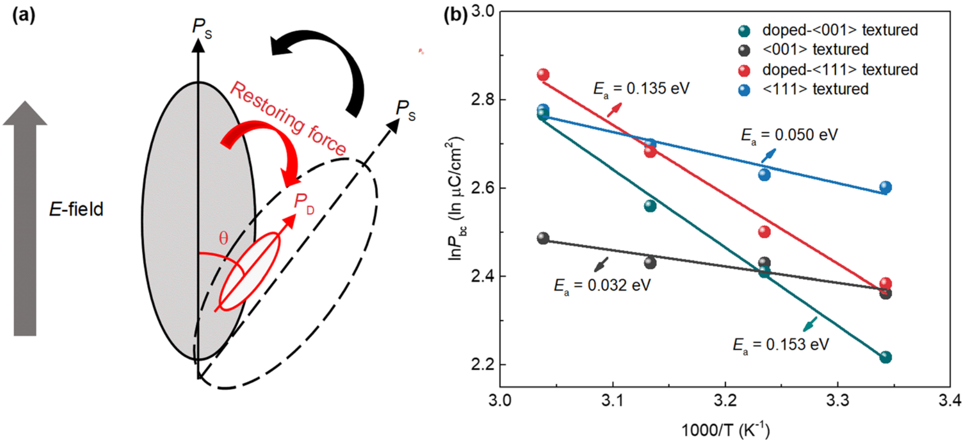

Fig. 8 (a) Schematic diagram of restricted polarization rotation induced by defect polarization P_D in acceptor-doped piezoelectric materials. (b) Plot of $\ln(P_{bc})$ *versus* inverse temperature for ⟨001⟩ and ⟨111⟩ textured and doped ⟨001⟩ and ⟨111⟩ textured ceramics.

temperature following the Arrhenius Law:[35,49,50]

$$P_{bc} = P_0 \exp\left(\frac{-E_a}{k_B T}\right) \tag{3}$$

where P_0 is the fitting constant and E_a is the activation energy of polarization switching. The activation energy is determined to be 0.153 eV and 0.135 eV for doped ⟨001⟩ and ⟨111⟩ textured ceramics, respectively, which is much higher than that of undoped ⟨001⟩ and ⟨111⟩ textured ceramics (0.032 eV and 0.050 eV, respectively), as shown in Fig. 8b, experimentally demonstrating the constrained P_S switching in MnO_2-doped textured ceramics. The constrained P_S switching will lead to low magnitude of mechanical loss tan γ (high Q_m).

In addition to the hardening effects induced by MnO_2 dopant, the different engineered domain configurations can also play an important role in affecting Q_m value. The poled ⟨111⟩ oriented sample exhibits monodomain configuration (1R), thus, the low mechanical loss and high Q_m can be expected. For poled ⟨001⟩ oriented sample, it exhibits four equivalent engineered domains (4R), leading to the enhanced polarization rotation and higher mechanical loss (lower Q_m). Thus, the doped ⟨111⟩ textured ceramics will possess much higher Q_m value in comparison with doped ⟨001⟩ textured ceramics (Fig. 9a). As shown in Fig. 9b, the doped ⟨001⟩ textured ceramics exhibit the high d_{33} and moderate Q_m value in comparison with ⟨111⟩ textured ceramics exhibiting low d_{33} and high Q_m. Since the ⟨110⟩ oriented sample exhibits the two equivalent engineered domains (2R), lying between ⟨001⟩ and ⟨111⟩ oriented samples (4R and 1R, respectively), it is expected that the doped ⟨110⟩ textured ceramics can exhibit good combination of d_{33} and Q_m.

3.4. Enhanced high-power vibration characteristics in ⟨001⟩ and ⟨111⟩-textured ceramics

To demonstrate the effectiveness of doped ⟨001⟩ and ⟨111⟩ textured ceramics in high-power applications, we measured the high-power piezoelectric vibration characteristics for both doped ⟨001⟩ and ⟨111⟩ textured ceramics under the transverse length (31) mode using a laser vibrometer, as shown in Fig. 10a. These vibration characteristics were then compared with that of the commercial hard PZT ceramic (APC 841). Fig. 10c and d show the vibration velocity as a function of the measured frequencies under the constant driving voltage of 5 V_{p-p}, 10 V_{p-p} and 20 V_{P-P} for doped ⟨001⟩ and ⟨111⟩ textured ceramics

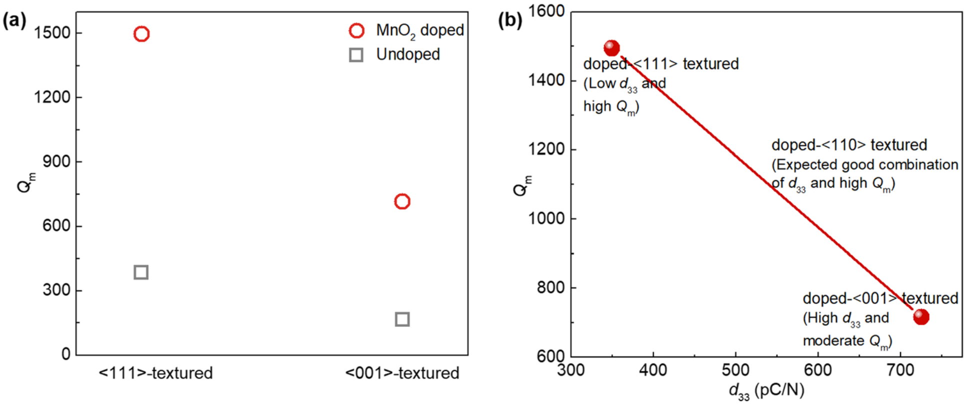

Fig. 9 (a) Q_m values of undoped and doped ⟨001⟩ and ⟨111⟩ textured ceramics. (b) Q_m *vs.* d_{33} for doped ⟨001⟩ and ⟨111⟩ textured ceramics.

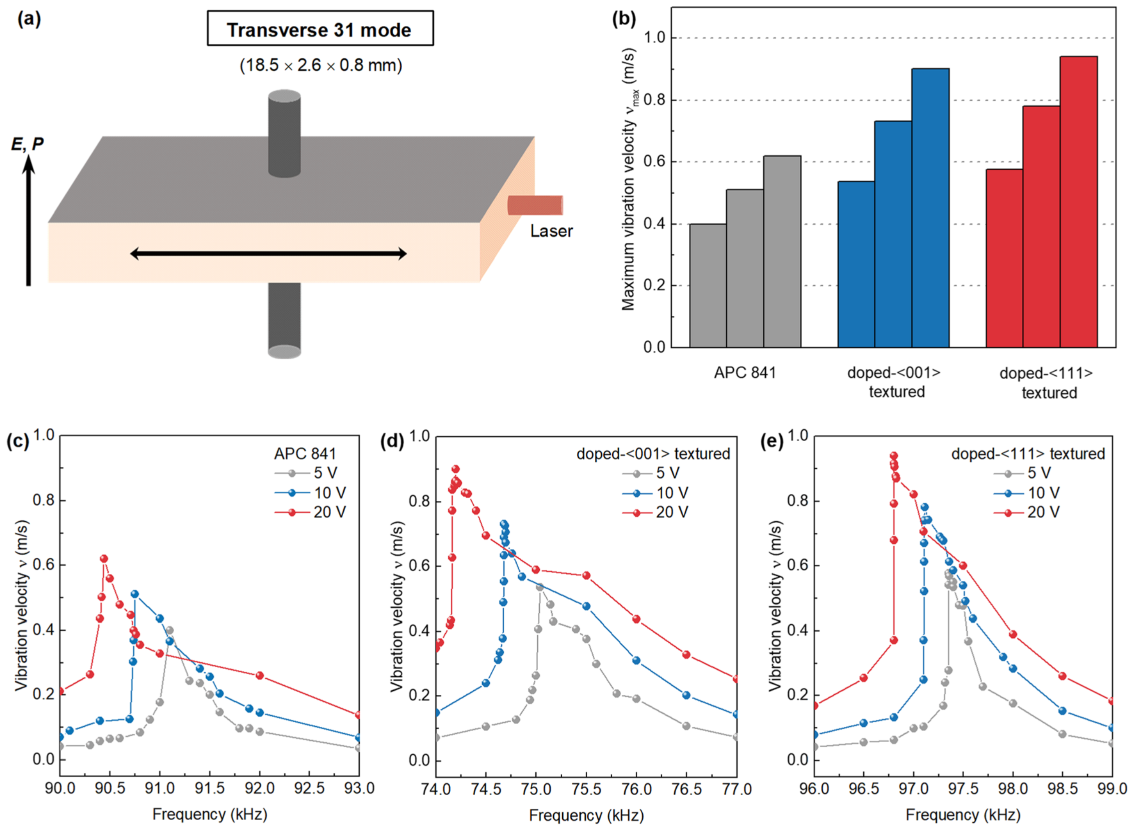

Fig. 10 (a) Schematics of the measured piezoelectric sample geometries (k_{31} mode), where electric field *E*, polarization *P*, and vibrometer laser beam directions are indicated by arrows. (b) Comparison of maximum vibration velocities at 5 V_{p-p}, 10 V_{p-p} and 20 V_{P-P} for APC 841, doped $\langle 001\rangle$ and $\langle 111\rangle$ textured ceramics. (c–e) Vibration velocity as a function of the measured frequency under the constant driving voltage of 5 V_{p-p}, 10 V_{p-p} and 20 V_{P-P} for APC 841, doped $\langle 001\rangle$ and $\langle 111\rangle$ textured ceramics, respectively (the measured vibration velocities of APC 841 are from ref. 18).

and APC 841 sample, respectively. The peak values of the measured vibration velocity at 5 V_{p-p}, 10 V_{p-p} and 20 V_{P-P} for these samples were compared in Fig. 10b. Under the same driving voltage, the maximum vibration velocity v_{max} of both $\langle 001\rangle$ and $\langle 111\rangle$ textured ceramics is much higher than that of the APC 841 sample. Specifically, the doped $\langle 001\rangle$ textured ceramic can exhibit around 1.5× higher v_{max} ($\sim$0.90 m s^{-1}) in comparison with commercial hard PZT samples ($\sim$0.62 m s^{-1}) at 20 V_{P-P}. The enhanced vibration velocity in doped $\langle 001\rangle$ textured ceramic can be understood in terms of its combinatory soft and hard piezoelectric properties, as shown in Table 1. Interestingly, a slightly higher v_{max} ($\sim$0.94 m s^{-1}) can be obtained in doped $\langle 111\rangle$ textured ceramic. Compared to both doped $\langle 001\rangle$ ceramic and APC 841 sample, the higher vibration velocity in doped $\langle 111\rangle$ textured ceramic should be attributed to its high Q_m and low elastic compliance s_{11} (Table 1) since the vibration velocity of piezoelectric ceramics is proportional to the figure of merit $\frac{d_{31}\cdot Q_m}{s_{11}^E}$.[13] It is known that the output power of high-power device is proportional to v^2. Thus, both doped $\langle 001\rangle$ and $\langle 111\rangle$ textured ceramics will show over 2× higher output power in comparison with APC 841 sample. The experimental results here clearly demonstrate the promise of doped $\langle 001\rangle$ and $\langle 111\rangle$ textured piezoelectric ceramics for replacing conventional random ceramics in high-power applications.

4. Conclusion

In summary, both $\langle 001\rangle$ and $\langle 111\rangle$ textured PIN–PMN–PT ceramics were successfully fabricated though TGG method to investigate the effects of the crystallographic orientation on high-power properties of PIN–PMN–PT ceramics. Interestingly, we found that both piezoelectric properties and mechanical quality factor exhibit crystallographic orientation dependent behavior in PIN–PMN–PT ceramics. The $\langle 001\rangle$ textured PIN–PMN–PT ceramics possess higher piezoelectric constant d_{33} and coupling factors k_{31} in comparison with both random and $\langle 111\rangle$ textured counterparts, while the mechanical quality factor Q_m was enhanced in $\langle 111\rangle$ textured ceramics due to the less favored polarization rotation in $\langle 111\rangle$ oriented sample with monodomain configuration (1R). The d_{33} of $\langle 001\rangle$ textured ceramics can be further improved from 412 pC N^{-1} to 725 pC N^{-1} because of the improved $\langle 001\rangle$ texturing degree and poling degree induced by MnO_2 doping. In addition, the Q_m values for $\langle 001\rangle$ and $\langle 111\rangle$ textured ceramics were significantly improved by MnO_2 doping effect. The doped $\langle 001\rangle$ textured ceramics exhibit high d_{33} and moderate Q_m (d_{33} = 725 pC N^{-1}, Q_m = 716) in comparison with $\langle 111\rangle$ textured ceramics exhibiting low d_{33} and high Q_m (d_{33} = 350 pC N^{-1}, Q_m = 1495). Compared to commercial hard PZT samples, the doped $\langle 001\rangle$ textured ceramics exhibit around 1.5× higher vibration velocity ($\sim$ 0.90 m s^{-1}), which is mainly attributed to its high soft and hard piezoelectric properties. In addition, owing to the high Q_m and low elastic compliance s_{11}, the doped ⟨111⟩ textured ceramics possess higher vibration velocity ($\sim$ 0.94 m s^{-1}). Our experimental results demonstrate the promise of textured piezoelectric ceramics to replace conventional random ceramics in high-power applications.

Conflicts of interest

There are no conflicts to declare.

Acknowledgements

Y. Y. and H. L. acknowledge the financial support from DARPA through award number HR00111920001. X. L. acknowledges the support through National Science Foundation through the award number DMR-1936432. S. K. K. acknowledges the support through National Science Foundation through the award number 1904811. S. P. acknowledges the support through USDA NIFA through grant number 2019-67021-28991.

References

1 Y. Chang, S. F. Poterala, Z. Yang, S. Trolier-McKinstry and G. L. Messinge, *J. Mater. Res.*, 2010, **25**, 687–694.

2 L. Chen, H. Liu, H. Qi and J. Chen, *Prog. Mater. Sci.*, 2022, **127**, 100944.

3 F. Li, S. Zhang, Z. Xu, X. Wei and T. R. Shrout, *Adv. Funct. Mater.*, 2011, 2118–2128.

4 S. Zhang, F. Li, X. Jiang, J. Kim, J. Luo and X. Geng, *Prog. Mater. Sci.*, 2015, **68**, 1–66.

5 F. Li, S. Zhang, T. Yang, Z. Xu, N. Zhang, G. Liu, J. Wang, J. Wang, Z. Cheng, Z. G. Ye, J. Luo, T. R. Shrout and L. Q. Chen, *Nat. Commun.*, 2016, **7**, 1–9.

6 X. Li, Z. Wang, C. He, X. Long and Z. G. Ye, *J. Appl. Phys.*, 2012, **111**, 034105.

7 S. Zhang, F. Li, N. P. Sherlock, J. Luo, H. Jae Lee, R. Xia, R. J. Meyer, W. Hackenberger and T. R. Shrout, *J. Cryst. Growth*, 2011, **318**, 846–850.

8 X. Liu, S. Zhang, J. Luo, T. R. Shrout and W. Cao, *Appl. Phys. Lett.*, 2010, **96**, 2008–2011.

9 Y. Chang, B. Watson, M. Fanton, R. J. Meyer and G. L. Messing, *Appl. Phys. Lett.*, 2017, **111**, 232901.

10 F. H. Schader, G. A. Rossetti, J. Luo and K. G. Webber, *Acta Mater.*, 2017, **126**, 174–181.

11 M. Slabki, J. Wu, M. Weber, P. Breckner, D. Isaia, K. Nakamura and J. Koruza, *J. Am. Ceram. Soc.*, 2019, **102**, 6008–6017.

12 K. Uchino, *Adv. Piezoelectr. Mater.*, 2010, 1–678.

13 H. Nagata and T. Takenaka, *Electron. Commun. Jpn.*, 2013, **96**, 53–58.

14 Y. Yan, K. H. Cho, D. Maurya, A. Kumar, S. Kalinin, A. Khachaturyan and S. Priya, *Appl. Phys. Lett.*, 2013, **102**, 0–5.

15 S. Yang, J. Li, Y. Liu, M. Wang, L. Qiao, X. Gao, Y. Chang, H. Du, Z. Xu, S. Zhang and F. Li, *Nat. Commun.*, 2021, **12**, 1–10.

16 D. D. Wei, Q. Bin Yuan, G. Q. Zhang and H. Wang, *J. Mater. Res.*, 2015, **30**, 2144–2150.

17 H. Leng, Y. Yan, H. Liu, M. Fanton, R. J. Meyer and S. Priya, *Acta Mater.*, 2021, **206**, 116610.

18 B. H. Watson, M. J. Brova, M. A. Fanton, R. J. Meyer and G. L. Messing, *J. Am. Ceram. Soc.*, 2020, **103**, 6319–6329.

19 E. Sun, R. Zhang, F. Wu, B. Yang and W. Cao, *J. Appl. Phys.*, 2013, **113**, 0–4.

20 H. Leng, Y. Yan, B. Wang, T. Yang, H. Liu, X. Li, R. Sriramdas, K. Wang, M. Fanton, R. J. Meyer, L.-Q. Chen and S. Priya, *Acta Mater.*, 2022, **234**, 118015.

21 Y. Yan, L. Yang, Y. Zhou, K. H. Cho, J. S. Heo and S. Priya, *J. Appl. Phys.*, 2015, **118**, 104101.

22 S. Su, R. Zuo, D. Lv and J. Fu, *Powder Technol.*, 2012, **217**, 11–15.

23 F. K. Lotgering, *J. Inorg. Nucl. Chem.*, 1960, **16**, 100–108.

24 Y. Chang, J. Wu, Z. Liu, E. Sun, L. Liu, Q. Kou, F. Li, B. Yang and W. Cao, *ACS Appl. Mater. Interfaces*, 2020, **12**, 38415–38424.

25 H. Y. Park, C. H. Nam, I. T. Seo, J. H. Choi, S. Nahm, H. G. Lee, K. J. Kim and S. M. Jeong, *J. Am. Ceram. Soc.*, 2010, **93**, 2537–2540.

26 J. Padilla and D. Vanderbilt, *Phys. Rev. B: Condens. Matter Mater. Phys.*, 1997, **56**, 1625–1631.

27 G. L. Messing, S. Trolier-McKinstry, E. M. Sabolsky, C. Duran, S. Kwon, B. Brahmaroutu, P. Park, H. Yilmaz, P. W. Rehrig, K. B. Eitel, E. Suvaci, M. Seabaugh and K. S. Oh, Templated grain growth of textured piezoelectric ceramics, *Crit. Rev. Solid State Mater. Sci.*, 2004, **29**, 45–96.

28 Z. Li, H. C. Thong, Y. F. Zhang, Z. Xu, Z. Zhou, Y. X. Liu, Y. Y. S. Cheng, S. H. Wang, C. Zhao, F. Chen, K. Bi, B. Han and K. Wang, *Adv. Funct. Mater.*, 2021, **31**, 2005012.

29 Q. Li, M. H. Zhang, Z. X. Zhu, K. Wang, J. S. Zhou, F. Z. Yao and J. F. Li, *J. Mater. Chem. C*, 2017, **5**, 549–556.

30 F. Z. Yao, K. Wang, W. Jo, J. S. Lee and J. F. Li, *J. Appl. Phys.*, 2014, **116**, 114102.

31 M. Cheng, Z. Fang, F. Li, Y. Zhang, Y. Qin, X. Wang, K. Zhang and X. Tian, *Ceram. Int.*, 2020, **46**, 13324–13330.

32 F. Li, L. Jin and R. Guo, *Appl. Phys. Lett.*, 2014, **105**, 0–4.

33 F. Li, D. Lin, Z. Chen, Z. Cheng, J. Wang, C. Li, Z. Xu, Q. Huang, X. Liao, L. Q. Chen, T. R. Shrout and S. Zhang, *Nat. Mater.*, 2018, **17**, 349–354.

34 F. Li, L. Jin, Z. Xu and S. Zhang, *Appl. Phys. Rev.*, 2014, **1**, 011103.

35 L. Zheng, L. Yang, Y. Li, X. Lu, D. Huo, W. Lü, R. Zhang, B. Yang and W. Cao, *Phys. Rev. Appl.*, 2018, **9**, 64028.

36 N. Luo, S. Zhang, Q. Li, Q. Yan, Y. Zhang, T. Ansell, J. Luo and T. R. Shrout, *J. Mater. Chem. C*, 2016, **4**, 4568–4576.

37 G. Liu, S. Zhang, W. Jiang and W. Cao, *Mater. Sci. Eng., R*, 2015, **89**, 1–48.

38 K. Uchino, J. H. Zheng, Y. H. Chen, X. H. Du, J. Ryu, Y. Gao, S. Ural, S. Priya and S. Hirose, *J. Mater. Sci.*, 2006, **41**, 217–228.

39 Y. Yan, L. D. Geng, L. F. Zhu, H. Leng, X. Li, H. Liu, D. Lin, K. Wang, Y. U. Wang and S. Priya, *Adv. Sci.*, 2022, **2105715**, 1–10.

40 A. M. González, Á. García, C. Benavente-Peces and L. Pardo, *Materials*, 2016, **9**, 72.

41 J. Fu, R. Zuo and Z. Xu, *Appl. Phys. Lett.*, 2011, **99**, 14–17.

42 J. Ma, K. Zhu, D. Huo, X. Qi, E. Sun and R. Zhang, *Appl. Phys. Lett.*, 2021, **118**, 3–8.

43 P. Li, Y. Huan, W. Yang, F. Zhu, X. Li, X. Zhang, B. Shen and J. Zhai, *Acta Mater.*, 2019, **165**, 486–495.

44 Y. M. Jin, Y. U. Wang, A. G. Khachaturyan, J. F. Li and D. Viehland, *Phys. Rev. Lett.*, 2003, **91**, 1–4.

45 W. Cao and C. A. Randall, *J. Phys. Chem. Solids*, 1996, **57**, 1499–1505.

46 Y. Yan, Y. Zhou and S. Priya, *Appl. Phys. Lett.*, 2014, **104** 1–6.

47 Z. Feng and X. Ren, *Phys. Rev. B: Condens. Matter Mater. Phys.*, 2008, **77**, 1–6.

48 X. Ren, *Nat. Mater.*, 2004, **3**, 91–94.

49 B. Ma, Z. Hu, S. Liu, M. Narayanan and U. Balachandran, *Appl. Phys. Lett.*, 2013, **102**, 0–4.

50 R. Nie, Q. Zhang, Y. Yue, H. Liu, Y. Chen, Q. Chen, J. Zhu, P. Yu and D. Xiao, *J. Appl. Phys.*, 2016, **119**, 124111.